PROGRESS TOWARDS A 3D AERODYNAMIC SHAPE OPTIMIZATION TOOL FOR THE COMPRESSIBLE, HIGH-*Re* NAVIER-STOKES EQUATIONS DISCRETIZED ON UNSTRUCTURED MESHES.

Jonathan Elliott*and Jaime Peraire†
Fluid Dynamics Research Laboratory
MIT Department of Aeronautics and Astronautics

Abstract

We report on recent progress towards the development of a 3D optimization capability for transonic flow at high Reynolds numbers. In this paper we demonstrate optimization based on the 3D laminar Navier-Stokes equation, and we present validation of the flow analysis scheme based on the 2D Navier-Stokes equations with turbulence modelling.

1 Introduction

The authors are involved in a project in which the long term goal is the development of an aerodynamic optimization tool (such as one that performs drag minimization at fixed lift) for vehicles immersed in 3D high-*Re* transonic/supersonic flow in which the discretization is performed on unstructured grids. Drag minimization has the advantage over traditional inverse design methods that the designer is relieved from the difficult task of selecting an appropriate target pressure distribution (he/she instead must choose an appropriate set of design variables and objective functions, but that arguably allows more freedom, and can be more easily related to the goals of the design project). Use of unstructured grids as the underlying flow analysis method for this optimization tool provides a powerful method for performing aerodynamic design for complex geometric configuration such as cruise wing design in the presence of strut-nacelles, wing design in high-lift mode and lateral-directional control configurations such as wings with deployed ailerons or spoilers.

Previous publications have documented various stages of the project [10, 11, 12, 13] in which *practical* capabilities have been developed for flow fields satisfying the 2D and 3D Euler equations and the 2D laminar Navier-Stokes equations. For example, an efficient residual jacobian storage scheme was reported in [11]. This paper reports on the extension of the method to an optimization method based on the 3D laminar Navier-Stokes equations and verifies that the residual jacobian storage scheme allows a *practical* capability. Furthermore, the 2D turbulent implementation is currently in progress and we present validation of the flow analysis module.

*Graduate Research Assistant, Member AIAA
†Associate Professor

Copyright ©1996 American Institute of Aeronautics and Astronautics, Inc. All rights reserved.

2 Algorithms

Flow Analysis

For illustration purposes, the algorithms are described based on the 2D algorithm. The 3D algorithm is a direct extension thereof. The starting point is the integral form of the Reynolds-averaged Navier-Stokes equations:-

$$\int_\Omega \frac{\partial \mathbf{U}}{\partial t} d\Omega = \int_\Omega \frac{\partial}{\partial x_j}(\mathbf{G}^j - \mathbf{F}^j) d\Omega = \oint_\Gamma (\mathbf{G}^j - \mathbf{F}^j) n_j d\Gamma \quad (1)$$

where $\mathbf{U} = (\rho, \rho u_1, \rho u_2, \rho E)^T$,

$$\mathbf{F}^j = \begin{bmatrix} \rho u_j \\ \rho u_1 u_j + p\delta_{1j} \\ \rho u_2 u_j + p\delta_{2j} \\ u_j(p + \rho E) \end{bmatrix}, \mathbf{G}^j = \begin{bmatrix} 0 \\ \tau_{1j} \\ \tau_{2j} \\ u_i \tau_{ij} + k_{tot} \frac{\partial T}{\partial x_j} \end{bmatrix} \quad (2)$$

and Ω is a closed control volume with boundary, Γ. Here τ_{ij} is the tensor of viscous stresses and is given by

$$\tau_{ij} = \mu_{tot} \left(\frac{\partial u_i}{\partial x_j} + \frac{\partial u_j}{\partial x_i} \right) - \frac{2}{3} \mu_{tot} \delta_{ij} \frac{\partial u_k}{\partial x_k}. \quad (3)$$

We have used the Boussinesq analogy for eddy viscosity and eddy conductivity and replaced the Reynolds stress and turbulent heat flux by a gradient diffusion term resulting in

$$k_{tot} = k + k_t$$
$$\mu_{tot} = \mu + \mu_t$$

We first assume that $\mathbf{G}^j = 0$ and present the underlying inviscid scheme. The discretization of $\mathbf{U}$ and $\mathbf{F}^j$ on an unstructured triangulation of the domain is accomplished using piecewise linear polynomials. The spatial discretization is completed by using the finite volume formulation with control volumes associated with each node i consisting of all triangles having vertex i. The line integration given by Equation (1) is performed exactly around the outer boundary of this control volume. Using this spatial discretization, the following set of semi-discrete equations results:-

$$\frac{d\mathbf{U}}{dt} + \mathbf{R}(\mathbf{U}) = \mathbf{0} \quad (4)$$

where, through the use of an edge-based formulation, the residual at node i can be written as

$$\mathbf{R}_i = \sum_{ik=1}^{K} [\mathbf{R}]_{ik}. \quad (5)$$

Here ik represents the edge connecting nodes i and k and the residual increment for an interior edge is given by,

$$[\mathbf{R}]_{ik} = \sum_j \frac{\mathbf{F}_i^j + \mathbf{F}_k^j}{2} S_{ik}^j - \mathbf{D}_{ik} \tag{6}$$

where S_{ik}^j is the area vector associated with edge ik and is calculated as follows:-

$$(S_{ik}^1, S_{ik}^2) = \left(\frac{x_{k+1}^2 - x_{k-1}^2}{3}, \frac{x_{k-1}^1 - x_{k+1}^1}{3} \right) \tag{7}$$

where $k+1$ and $k-1$ are the nodes in either element containing edge ik different from i and k. The second term on the right hand side in Equation (6) is an artificial dissipation flux added to stabilize the scheme and is given by:-

$$\mathbf{D}_{ik} = \frac{S}{2} \mathbf{P} |\mathbf{\Lambda}| (\mathbf{P}^{-1} \Delta \mathbf{U}_{ik} - L(\mathbf{P}^{-1} \Delta \mathbf{U}^-, \mathbf{P}^{-1} \Delta \mathbf{U}^+)) \tag{8}$$

Here $\Delta \mathbf{U}^-$ and $\Delta \mathbf{U}^+$ represent changes in $\mathbf{U}$ along an imaginary line segment extended past the positive and negative ends of the edge, of equal length and direction to those of the edge itself, $x_k^j - x_i^j$. $L(u,v)$ in Equation (8) is a nonlinear averaging function, constructed to retain coefficient positivity for the characteristic differences, $\Delta \mathbf{W}^{\pm} = \mathbf{P}^{-1} \Delta \mathbf{U}^{\pm}$, and therefore the LED-like character of the numerical scheme [20, 12]. It should be noted that if an exact average is returned by $L(u,v)$, then the combination of characteristic differences inside the paranthesis in Equation (8) can be seen to form a third order dissipative flux. (Note that $\mathbf{P}$ is the matrix of eigenvectors and $\mathbf{\Lambda}$ is the matrix of eigenvalues for the Roe matrix, $\mathbf{A}(\mathbf{U}_i, \mathbf{U}_k)$ based on the unit normal associated with S_{ik}^j and $\mathbf{A}$ incorporates the Harten correction [18] to avoid zero eigenvalues.)

The terms $\Delta \mathbf{U}^-$, $\Delta \mathbf{U}^+$ are calculated from the nodal gradients, which in turn are calculated using the finite volume formulation resulting in

$$\frac{\partial \mathbf{U}_i}{\partial x^j} = \frac{1}{V_i} \left(\sum_{il=1}^{\mu_i} \frac{\mathbf{U}_i + \mathbf{U}_l}{2} S_{il}^j + \sum_{il=1}^{n_{bou}} \frac{5\mathbf{U}_i + \mathbf{U}_l}{4} S_{il}^l \right) \tag{9}$$

where μ_i is the number of nodes neighbouring node i, n_{bou} is the number of boundary edges contributing to the residual at node i and subscript il represents the edge connecting nodes i and l. For this form of gradient evaluation, the rigourous LED character of the scheme is lost but for transonic and low supersonic flows this scheme tends to produce smoother and less dissipative solutions than schemes previously reported by the authors for inviscid flow [12, 13].

The means for inclusion of viscous terms recycles the nodal gradients used for the dissipative fluxes. The flux, $\mathbf{F}_i^j$, for example, in Equation (6) is simply replaced by $\mathbf{F}_i^j - \mathbf{G}_i^j$.

It was found desirable to use a smoother limiter function than the previously-reported standard minmod limiter for Euler flows in Equation (8), to avoid the limiter switching to first order in regions of high curvature, such as the edge of the boundary layer. The limiter used was that employed in [17] and is

$$L(u,v) = minmod(2u, 2v, \frac{u+v}{2}). \tag{10}$$

Note that this limiter is more likely to return the third argument, and by examination of Equation (8), results in a scheme with a desirable third order dissipative flux.

Turbulence Modelling

Two turbulence models were considered: the Cebeci-Smith [5, 22] and Spalart-Allmaras [25] models. For the calculations based on the Cebeci-Smith turbulence model, the eddy viscosity in the inner layer is found using the mixing length hypothesis with

$$\begin{aligned} \mu_t &= \rho l_{mix}^2 \left\{ \left(\frac{\partial u_1}{\partial x_2} \right)^2 + \left(\frac{\partial u_2}{\partial x_1} \right)^2 \right\}^{1/2} \\ l_{mix} &= \kappa y \left[1 - \frac{y u_\tau}{\nu A^+} \right]. \end{aligned}$$

where the standard notation has been used. The reader is referred to the original texts for the definitions of these symbols. In the outer layer,

$$\mu_t = \alpha \rho U_e \delta_v^* F_{Kleb}(y, \delta)$$

where F_{Kleb} is a function that is given in [5]. As shown in [28], y_m^+, the dividing line between inner and outer layers is given by

$$y_m^+ \approx 0.04 Re_{\delta^*}$$

For calculations using the Spalart-Allmaras model, an additional partial differential equation in a variable related to the eddy viscosity is solved. The equation is given by

$$\begin{aligned} \frac{D\tilde{\nu}}{Dt} &= c_{b1}[1 - f_{t2}]\tilde{S}\tilde{\nu} + \frac{1}{\sigma} \left[\nabla \cdot ((\nu + \tilde{\nu}) \nabla \tilde{\nu}) + c_{b2} (\nabla \tilde{\nu})^2 \right] \\ &\quad - \left[c_{w1} f w - \frac{c_{b1}}{\kappa^2} \right] \left[\frac{\tilde{\nu}}{d} \right]^2 + f_{t1} \Delta U^2 \end{aligned} \tag{11}$$

where $\nu_t = \mu_t / \rho = \tilde{\nu} f_{v1}$. The reader is referred to the original paper for details of these terms [25]. In the current discretization we use the integral approach whereby, for example

$$\begin{aligned} \int_\Omega \frac{\partial \tilde{\nu}}{\partial t} + u_j \frac{\partial \tilde{\nu}}{\partial x_j} d\Omega &= \int_\Omega \frac{\partial \tilde{\nu}}{\partial t} - \tilde{\nu} \frac{\partial u_j}{\partial x_j} d\Omega + \oint_\Gamma (u_j \tilde{\nu}) n_j d\Gamma \\ &\approx \Omega_i \left[\frac{\partial \tilde{\nu}}{\partial t} - \tilde{\nu} \frac{\partial u_j}{\partial x_j} \right] + \sum_{ik=1}^{K} \tilde{\nu} u_j S^j. \end{aligned}$$

A first order discretization of the convective fluxes is then implemented by including a dissipative flux of the form $|\tilde{\gamma}|(\tilde{\nu}_i - \tilde{\nu}_k)$, where $\tilde{\gamma}$ is an approximation of the Roe-averaged advective contravariant velocity $\tilde{\gamma} \approx \vec{u}_i \cdot \hat{n}$ with the Harten correction [19] to maintain non-zero dissipation in regions where the contravariant velocity tends to zero. The 1st order discretization is desirable in order to prevent overshoots which could result in negative eddy viscosities.

Mesh Movement

For the Navier-Stokes calculations reported herein, we use a scheme in which the grid movement at a location x_j is

simply given by the sum of the airfoil surface modal perturbations corresponding to that value of x_1. This eliminates the potential problem of negative volume elements in the perturbed grid in the boundary layer due to the small mesh spacing in the normal direction. This will obviously have to be dealt with in a more satisfactory manner when extending to multi-element airfoils and 3D Navier-Stokes.

Sensitivity Analysis

Two methods of performing sensitivity analysis have been used herein, both based on the discrete sensitivity analysis approach [12, 13]. For all the optimization examples, the adjoint approach was used in which the adjoint variable ψ is calculated by solving

$$\left[\frac{\partial \mathbf{R}}{\partial \mathbf{U}}\right]^T \psi = -\left\{\frac{\partial I}{\partial \mathbf{U}}\right\}^T \tag{12}$$

and the cost function sensitivities are calculated from

$$\left.\frac{dI}{d\beta}\right|_{\mathbf{R}=0} = \frac{\partial I}{\partial \beta} + \psi^T \left\{\frac{d\mathbf{R}}{d\beta}\right\} \tag{13}$$

For some sensitivity validation exercises, the direct method was used in which the local state vector sensitivity, $\partial \mathbf{U}/\partial \beta$ is calculated by solving

$$\frac{\partial \mathbf{R}}{\partial \mathbf{U}}\frac{\partial \mathbf{U}}{\partial \beta} = -\frac{\partial \mathbf{R}}{\partial \beta} \tag{14}$$

and the cost function sensitivity is calculated from

$$\left.\frac{dC_{D_j}}{d\beta}\right|_{\mathbf{R}=0} = \frac{\partial C_{D_j}}{\partial \beta} + \frac{\partial C_{D_j}}{\partial \mathbf{U}}\frac{\partial \mathbf{U}}{\partial \beta}. \tag{15}$$

Time Integration

Time integration was performed using the same time integration scheme as that for flow analysis, that is, by introducing a pseudo-unsteady term into for example the adjoint equation [12, 13]

$$\frac{d\psi}{dt} + \left[\frac{\partial \mathbf{R}}{\partial \mathbf{U}}\right]^T \psi - \left[\frac{\partial C_{D_j}}{\partial \mathbf{U}}\right]^T = 0 \tag{16}$$

For the Navier-Stokes flow analysis calculations it was felt that an implicit scheme was needed due to the small sizes of the elements in the boundary layer in the normal direction. For low-Re laminar calculations, a point implicit timestepping algorithm scheme was used. It was found to allow at least a doubling of the asymptotic convergence rate for one fourth of the per-iteration CPU cost of the multistage scheme for the adjoint calculation. For a given problem we always use the same time marching algorithm for both flow and adjoint analysis. For high-Re turbulent calculations, a preconditioned multi-stage timestepping scheme was used similar to that reported in [1, 21].

The point implicit algorithm follows the ideas elucidated in [17, 16], but differs in that the exact block diagonal entries of the $\partial \mathbf{R}/\partial \mathbf{U}$ matrix are used on the left hand side as opposed to only the first order terms. In brief, the relaxation scheme is

$$\mathbf{L}_i \Delta \mathbf{U}_i = (\Omega_i + \Delta t_i \left.\frac{\partial \mathbf{R}}{\partial \mathbf{U}}\right|_{ii})\Delta \mathbf{U}_i = \Delta t_i \mathbf{R}_i \tag{17}$$

where

$$\mathbf{U}_i^{n+1} = \mathbf{U}_i^n + \Delta \mathbf{U}_i. \tag{18}$$

Finally, a viscous correction was made to the Δt_i in an effort to ensure that the viscous time step limit is not exceeded, thereby compromising stability. This correction is given by

$$\Delta t_i = \frac{\Delta t_i^{inv}}{1 + 4/Re_{\Delta s_i}} \tag{19}$$

where Δt_i^{inv} is the time step limit found using linearized Fourier analysis for the inviscid scheme [14] and $Re_{\Delta s_i}$ is the Reynolds number based on the length of the smallest edge in the elements surrounding node i. It has been found by many researchers that this stability limit can have a large influence for well-resolved, low Reynolds number flows.

Jacobian storage

Efficient storage of $\partial \mathbf{R}/\partial \mathbf{U}$ can be performed by calculating the jacobian in two stages. The residual contribution for a given edge can be written as

$$\mathbf{R}(\mathbf{U}) = \mathbf{R}(\mathbf{U}, \mathbf{U}_{x_i}; \mathbf{U}) \tag{20}$$

Following previous work, e.g.[3], we apply the chain rule and obtain,

$$\begin{aligned} \frac{d\mathbf{R}}{d\mathbf{U}} &= \frac{\partial \mathbf{R}}{\partial \mathbf{U}}_I + \frac{\partial \mathbf{R}}{\partial \mathbf{U}}_{II} \\ &= \frac{\partial \mathbf{R}}{\partial \mathbf{U}}_I + \frac{\partial \mathbf{R}}{\partial \mathbf{U}_{x_j}}\frac{\partial \mathbf{U}_{x_j}}{\partial \mathbf{U}} \end{aligned}$$

where we have used the shorthand $\mathbf{U}_{x_j} = \partial \mathbf{U}/\partial x_j$. This doesn't appear to be much of a savings since $\partial \mathbf{U}_{x_j}/\partial \mathbf{U}$, at first glance, appears to be quite large. However, it is quickly found after examining the expression used to calculate $\mathbf{U}_{x_j}$, that each conservative variable component is only dependent on neighbouring nodal values of that same conservative variable component. Therefore $\partial \mathbf{U}_{x_j}/\partial \mathbf{U}$ is only nonzero if the same conservative variable components are being compared. Also $\partial \mathbf{U}_{x_j}/\partial \mathbf{U}$ is the same for all conservative variable components. Therefore $\partial \mathbf{U}_{x_j}/\partial \mathbf{U}$ is quite small (on the order of $100N_{point}$ while $\partial \mathbf{R}/\partial \mathbf{U}_I$ is on the order $600N_{point}$, for example), and $\partial \mathbf{R}/\partial \mathbf{U}$ can be stored using about the same amount of memory as was required to store the Euler residual jacobian based on the small-stencil scheme reported in [12, 13].

Optimization Strategy

A subspace BFGS algorithm is used to minimize drag with constraints on lift for both examples discussed herein. The algorithm is presented in [13, 9], and here we give only

a brief description. An increasingly accurate estimate to the Hessian (of the cost function with respect to the design variables) is developed in the subspace, $\mathbf{Z}$, orthogonal to the constraint gradients. This estimate is based on the usual BFGS formula, but uses variables which are all projected into the subspace [15]. The matrix $\mathbf{Z}_k$ which is used to perform the projection is found by performing an LQ decomposition of the constraint gradients, $\partial C_L/\partial\beta_j$. This formulation requires the solution of two adjoint problems per line search – one for C_L and one for C_D. The method appears to be quite robust since, as for the unconstrained BFGS algorithm, the Hessian approximation is guaranteed to remain positive definite provided the exact Hessian is positive definite and provided sufficient progress is made towards the minimum for each line search [15].

3 Validation

3D NACA0012 laminar flow analysis A calculation was performed for a two-dimensional wing, formed by extruding the NACA0012 airfoil in the spanwise direction, with freestream conditions of $M = 0.8, \alpha = 3.5°, Re = 2000$. The grid is shown in Figure 1. The C_p and M distributions are shown in Figures 2 and 3. The surface C_p distributions are compared with the corresponding distributions as found along the displacement surface by MSES [7] in Figure 4. Both surfaces exhibit good agreement and boundary layer quantities such as δ^* and C_f (not shown) also agree well.

3D NACA0012 sensitivity analysis Sensitivity calculations were performed based on the solution described above. Comparisons (finite difference versus analytic derivative) of the resulting surface $\partial\rho/\partial\beta$ and $\partial\rho E/\partial\beta$ distributions are shown for the angle of attack design variable (Figures 5, 7) and a NACA 4-series meanline mode design variable (Figures 6, 8) revealing good agreement. The adjoint sensitivity module has been fully validated versus finite difference. Table 1 shows the results for the parallel version of the code using only C_l as the cost function. As reported for the corresponding 2D cases [13], quite good agreement is found for α while the discrepancies for the camber mode are believed to be due to the finite difference step size used in making that estimate. $\Delta\beta_c = 0.001$ was used corresponding to a movement in the airfoil surface of 0.1% of chord. As pointed out in reference [13], the very close agreement between distributions of $\partial p/\partial\beta$ (shown in Figure 6) and $\partial\tau_{11}/\partial\beta$ (not shown) as calculated by finite difference and direct methods, indicates that the analytic derivatives are the more accurate, since these quantities are the only ones that contribute to the body forces. Therefore, the slight disagreements observable in Figure 6 due to the size of the finite difference step, is presumably the source of error. Further tests in the course of the optimization exercises by comparison of $\Delta\beta_j\partial C_l/\partial\beta_j$ with ΔC_l and $\Delta\beta_j\partial C_d/\partial\beta_j$ with ΔC_d provided further definitive evidence in this regard.

β	$\partial C_l/\partial\beta\vert_{FD}$	$\partial C_l/\partial\beta\vert_{AD}$
α	0.03943	0.03917
camber	-0.3296	-0.3700

Table 1: Comparison of 3D sensitivities to α and NACA 4-series meanline mode

Turbulent flat plate flow analysis The grid used is shown in Figure 9. No slip boundary conditions are applied along the lower boundary from $x = 0$ to $x = 1.5$; free slip boundary conditions are applied on the lower boundary from $x = -1.5$ to $x = 0$; non-reflecting Riemann boundary conditions are applied at the left boundary; pressure is specified while the appropriate characteristic variables are extrapolated from the interior along the top and right boundaries. Flow is from left to right. The freestream conditions are $Re = 5 \times 10^6$ and $M_\infty = 0.3$.

This test case or variations of it have been extensively tested by the authors and other researchers [23, 2, 26, 11] for laminar flows. For turbulent flows, at sufficiently large distances from the leading edge, the boundary layer profile is expected to exhibit log-law behaviour.

The profiles found at $x = 0.96$ using Spalart-Allmaras and Cebeci-Smith turbulence models are shown in Figure 11. It can be seen that good agreement with the Spalding composite law [27] is found for both models. Eddy viscosity and axial momentum distributions found for the Spalart-Allmaras solution are shown Figures 10-12. These are in good agreement with the distributions found for the Cebeci-Smith calculations (not shown), discrepancies in the eddy viscosity distributions being mostly restricted to the outer part of the boundary layer. Note that the trip terms were removed from the Spalart-Allmaras model for this calculation.

4 Results

The example demonstrating the extension of the 2D laminar optimization capability to 3D uses the ONERA M6 wing as a baseline geometry. The baseline flowfield is similar to those found for a 2D optimization case presented in a previous paper [11] and similar geometry and flowfield evolutions are observed in the course of the optimization exercise. Therefore it was felt appropriate to summarize the 2D optimization exercise here as well, for comparison purposes.

2D Attached Viscous Optimization Case The baseline geometry was a very thin airoil (with about 1% maximum thickness), with a thickness distribution that had already undergone considerable design and optimization for low Reynolds number viscous flow, albeit at a slightly higher Re=10000. The original airfoil is under consideration for

use in micro unmanned aerial vehicles (μ-UAVs). It had significant camber, but it was decided that a well behaved zero-camber airfoil was required as an initial test for the optimization system, so the camber was removed from the airfoil by a simple geometric operation. At $\alpha = 3.5°$, $M = 0.8$, and $Re = 2000$ it was found that the boundary layer C_f distribution was well above zero everywhere. The high Mach number was chosen, not for its realism in representing the flight conditions of μ-UAVs, but because it allows quicker convergence of the flow analysis calculations. It was decided that drag minimization with a lift constraint was an appropriate initial test, even though not much of a drag reduction was expected. The design variables were chosen to be the modal amplitudes of Hicks-Henne camber functions of the form $\Delta y(x) = \sin(\pi x^p)$ or $\Delta y(x) = \sin(\pi(1-x)^p)$with p chosen to be such that peaks occur at 20%, 40%, 60% and 80% of chord. In addition, the angle of attack was chosen as a design variable.

The baseline grid and Mach distribution are shown in Figures 13 and 15. The baseline grid contains 8506 nodes and at the trailing edge there are approximately 20 points in the boundary layer. The surface C_p distribution was found to match that found by MSES quite closely. Note that although there is locally supersonic flow, no shocks are present, although the ability to capture these shocks is an inherent part of the flow analysis algorithm.

The evolution of C_p distribution and geometry are shown in Figures 13-16. It can be seen that the minimum appears to have been almost reached after about 4 line searches which is about what should be expected for a well behaved design surface. The cost function has only decreased by 18 counts or about 2.2% of the baseline C_d. This modest decrease was expected since the baseline solution exhibited quite healthy boundary layer behaviour. Note that the decrease has come about partially by a reduction of the leading edge pressure peak. The resulting reduction in the net pressure increase and adverse pressure gradient along the upper surface causes the momentum thickness to be lower at the upper surface trailing edge, indicating a more healthy boundary layer and lower drag.

Also it should be noted that this optimization exercise was reproduced using MSES and and LINDOP, its associated optimization driver [8]. A similar reduction in C_d was observed, although the final geometry was slightly different. It is believed that this is due to the relatively shallow minimum.

3D ONERA M6 Wing The baseline geometry was the ONERA M6 wing. This wing has no camber and is untwisted. The nondimensional airfoil sections that the wing is lofted from are uniform across the span and have quite a large maximum thickness of $t/c_{max} = 9.7\%$. Therefore some separation is likely and indeed is found on the upper surface at the baseline conditions of $\alpha = 3.5°$, $M = 0.8$, and $Re = 1600$ based on the root chord. However it is limited to the aft 10%-20% of the airfoil and therefore the design space was expected to be rather smooth. It was decided that drag minimization with a lift constraint was an appropriate test, even though, once again, not much of a drag reduction was expected.

The design variables were product combinations of two chordwise functions and five spanwise functions whereby the surface geometry change is given by

$$\begin{aligned} z_{upper}(x,y) &= z^0_{upper}(x,y) + \textstyle\sum_{i=1}^{N_{des}} \beta_i h_i(x,y) \\ z_{lower}(x,y) &= z^0_{lower}(x,y) + \textstyle\sum_{i=1}^{N_{des}} \varphi_i \beta_i h_i(x,y). \end{aligned}$$

Here φ_k is -1 and 1 for thickness and camber design variables, respectively and z^0_{upper}, for example, represents the baseline upper surface. The chordwise functions, $f_i(x/c)$ and spanwise functions, $e_j(y)$ are summarized in Table 2. In addition, the angle of attack was chosen as a design variable.

func	definition	range
f_1	$\sin(\pi(x/c))$	$0 < x/c < 1$
f_2	x/c	$0 < x/c < 1$
e_1	$(y_1 - y)/(y_1 - y_0)$	$y_0 < y < y_1$
e_2	$(y - y_0)/(y_1 - y_0)$	$y_0 < y < y_1$
	$(y_1 - y)/(y_2 - y_1)$	$y_1 < y < y_2$
e_3	$(y - y_1)/(y_2 - y_1)$	$y_1 < y < y_2$
	$(y_2 - y)/(y_3 - y_2)$	$y_2 < y < y_3$
e_4	$(y - y_2)/(y_3 - y_2)$	$y_2 < y < y_3$
	$(y_3 - y)/(y_4 - y_3)$	$y_3 < y < y_4$
e_5	$(y - y_3)/(y_4 - y_3)$	$y_3 < y < y_4$

var	α	h_2	h_3	h_4	h_5
defn	—	f_1e_1	f_1e_2	f_2e_2	f_1e_3
var	h_6	h_7	h_8	h_9	h_{10}
defn	f_2e_3	f_1e_4	f_2e_4	f_1e_5	f_2e_5

Table 2: Surface Parameterization for viscous wing problem

The baseline grid, pressure distribution and Mach distribution are shown in Figures 17 to 19. The baseline grid contains 101,900 nodes and 578,880 tetrahedra. The grid was generated using HYPGEN [6], the grid generation program associated with OVERFLOW [4]. Each hexahedral cell in this structured grid was divided into six tetrahedra At the trailing edge there are approximately 12 points in the boundary layer. It should be noted that the gradient contributions, via $\partial\mathbf{R}/\partial\mathbf{G}\,\partial\mathbf{G}\partial\mathbf{U}$ were removed from $\mathbf{L}$ in Equation (17) since it was found that fluctuations in the result of the minmod limiter were destabilizing in the early stages of the calculation. Good convergence was found using $\sigma = 2.5$ and $\nu = 2.0$. Note that although there is locally

supersonic flow, no shocks are present, although the ability to capture these shocks is an inherent part of the flow analysis algorithm, as before.

The constrained BFGS algorithm described above was used to minimize C_D at the baseline C_L. The final C_p distribution is shown in Figures 20 while the evolution of geometry, C_p, C_f and θ distributions are shown in Figures 21 to 24. The minimum has been practically reached after 4 line searches.

Much of the behaviour observed for this case is similar to that observed for the 2D case discussed in Section 5.1.1. This might have been expected since similar design variables were utilized and minimal separation is present. Firstly, the cost function has only decreased by a small amount — in this case, 4 counts or about 0.4% of the baseline C_D, whereas the 2D case resulted in an 18-count reduction. The smaller decrease may be due to the lower number of camber design variables per section for the 3D case — just one was used per span station, whereas in the 2D case, four were used. As for the 2D case, this modest decrease was expected since the baseline solution exhibited quite healthy boundary layer behaviour. Another similarity to the 2D case is that the decrease has come about partially by a reduction of the leading edge pressure peak. The resulting reduction in the net pressure increase and adverse pressure gradient along the upper surface causes the momentum thickness to be lower at the upper and lower surface trailing edge — as can be seen in Figure 24 — indicating a more healthy boundary layer and lower sectional drag for each section. Indeed analysis using the Squire-Young formula [24] based on boundary layer quantities at the trailing edge at four sample span stations indicated profile drag decreases at each section. Induced drag was not examined. Unlike the 2D NACA0012 case, little change in the separation point at any section was observed.

5 Conclusion

A previously reported 2D laminar optimization capability has been successfully extended to three dimensions. Validation of the sensitivity calculation method using both adjoint and direct method was performed. Subsequently, a lift-constrained drag minimization exercise using the ONERA M6 as the baseline geometry was performed. The mostly-attached flow features resulted in a predictably similar geometry and flowfield evolution to an example performed in 2D which also possessed mostly-attached boundary layers. The residual jacobian storage scheme previously demonstrated in 2D was found to extend to 3D and result in practical memory costs based on a parallel implementation. The optimization example required approximately 80 hours of clock CPU time using 13 nodes on an SP2 to complete (for total of 1000 CPU-hours), indicating a practical 3D laminar optimization capability.

The extension to high-Re 2D turbulent flows is currently in progress. Validation (for flat plate solutions) of the flow analysis module associated with this capability is included.

Acknowledgements

We would like to express our thanks to Professor Mark Drela for continuing invaluable assistance at various stages of this project. The authors would like to thank the Flight Test Information Systems Branch of the NASA Dryden Research Center (under grant NAG4-100) and the Aerothermodynamics Branch of the NASA Langley Research Center (under grant NAG-1-1587) for partially supporting this research.

References

[1] S. R. Allmaras. Analysis of a Local Matrix Preconditioner for the 2D Navier-Stokes Equations. AIAA-93-3330CP, 1993.

[2] S. R. Allmaras. Contamination of Laminar Boundary Layers by Artificial Dissipation in Navier-Stokes Solutions. In *Proc. of the ICFD Conference on Numerical Methods for Fluid Dynamics*, Reading, England, UK, 1992.

[3] R. Beam and R. Warming. An Implicit Factored Scheme for the Compressible Navier-Stokes Equations. *AIAA Journal*, pages 393–402, April 1978.

[4] P. Buning, C. W.M., R. K.J., D. Sondat, I. Chiu, and S. J.P. OVERFLOW User's Manual Version 1.6. Technical report, NASA Ames.

[5] T. Cebeci and A. Smith. *Analysis of Turbulent Boundary Layers*. Academic Press, Inc, Orlando, FL, 1974.

[6] W. Chan, C. I., and P. Buning. User's Manual for the HYPGEN Hyperbolic Grid Generator and the HGUI Graphical User Interface. TM 108791, NASA, October 1993.

[7] M. Drela. Newton Solution of Coupled Viscous/Inviscid Multielement Airfoil Flows. AIAA-90-1470, 1990.

[8] M. Drela. Design and Optimization Method for Multi-Element Airfoils. *AIAA*, 93-0969, 1993.

[9] J. Elliott. *Aerodynamic Optimization based on the Euler and Navier-Stokes equations using Unstructured Grids*. PhD thesis, Dept. of Aeronautics and Astronautics, MIT, May, 1998.

[10] J. Elliott and J. Peraire. Aerodynamic Design using Unstructured Meshes. AIAA-96-1941, 1996.

[11] J. Elliott and J. Peraire. Aerodynamic Optimization using Unstructured Meshes with Viscous Effects. *AIAA*, 97-1849, 1997.

[12] J. Elliott and J. Peraire. Practical 3D Aerodynamic Design and Optimization using Unstructured Meshes. *AIAA Journal*, 35(9):1479–1485, 1997.

[13] J. Elliott and J. Peraire. Three-Dimensional, Multipoint, Lift-Constrained Drag Minimization using Unstructured Meshes. *Aeronautical Journal of the Royal Aeronautical Society*, accepted for publication, 1998.

[14] M. Giles. An Energy Stability Analysis of Multi-step Methods on Unstructured Meshes. Technical Report 87-1, MIT CFD Lab, 1987.

[15] P. E. Gill, W. Murray, and M. H. Wright, editors. *Practical Optimization*. Academic Press, 1981.

[16] P. Gnoffo, R. Candless, and H. Yee. Enhancements to Program Laura for Computation of Three-Dimensional Hypersonic Flow. AIAA Paper 87-0280, January 1987.

[17] P. A. Gnoffo. An Upwind-Biased Point-Implicit Relaxation Algorithm for Viscous, Compressible Perfect Gas Flows. TP 2953, NASA, February 1990.

[18] A. Harten and J. Hyman. Self adjusting grid methods for one-dimensional hyperbolic conservation laws. *Journal of Computational Physics*, 50:235–269, 1983.

[19] C. Hirsch. *Numerical Computation of Internal and External Flows, Vol.2*. John Wiley and Sons, Chichester, England, 1990.

[20] A. Jameson. Artificial Diffusion, Upwind Biasing, Limiters and their Effect on Accuracy and Multigrid Convergence in Transonic and Hypersonic Flows. AIAA-93-3359, 1993.

[21] A. Jameson, N.A.Pierce, and L.Martinelli. Optimum Aerodynamic Design Using the Navier-Stokes Equations. AIAA-97-0110, January 1997.

[22] S. Kline, M. V. Morkovin, G. Sovran, and D. J. Cockrell. A Finite-Difference Solution of the Incompressible Turbulent Boundary Layer Equations by an Eddy Viscosity Concept. In *Computation of Turbulent Boundary Layers — 1968 AFOSR-IFP Stanford Conference*, pages 346–355, 1968.

[23] J. Peraire, K. Morgan, M. Vahdati, and J. Peiro. The Construction and Behaviour of Some Unstructured Grid Algorithms for Compressible Flows. In *Proc. of the ICFD Conference on Numerical Methods for Fluid Dynamics*, Reading, England, UK, 1992.

[24] H. Schlichting. *Boundary Layer Theory*. McGraw–Hill, New York, 7th ed. edition, 1987.

[25] P. Spalart and S. Allmaras. A One-Equation Turbulence Model for Aerodynamic Flows. AIAA Paper 92-0439, 1992.

[26] S. Tatsumi, L. Martinelli, and A. Jameson. Flux-Limited Schemes for the Compressible Navier-Stokes Equations. *AIAA Journal*, 33:252–261, 1995.

[27] F. M. White. *Viscous Fluid Flow*. McGraw–Hill, New York, NY, 2nd edition, 1991.

[28] D. C. Wilcox. *Turbulence Modelling for CFD*. DCW Industries, Palm Drive, CA, 1st edition, 1993.

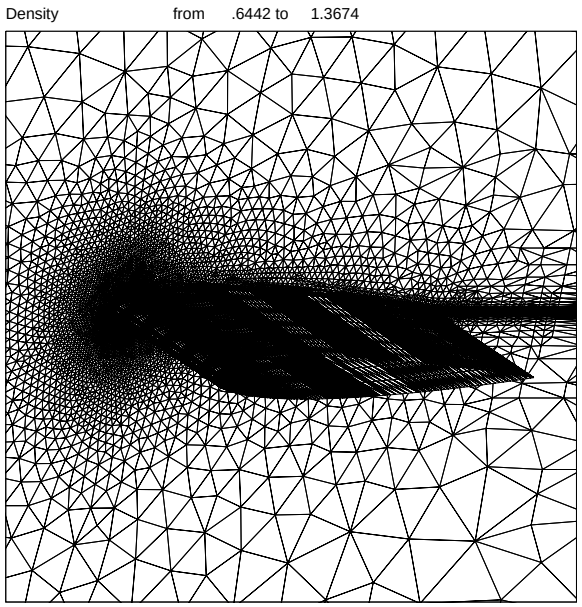

Figure 1: Grid used for 3D NACA0012 calculations

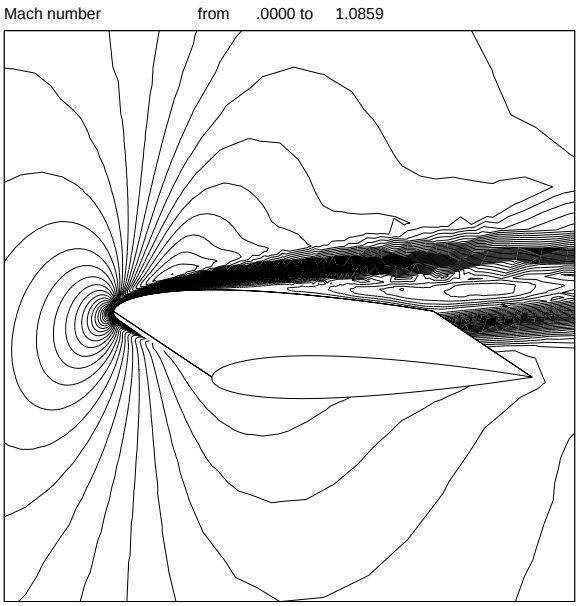

Figure 3: M distribution for NACA0012, Re=2000, $M_\infty = 0.8$, $\alpha = 3.5$ deg

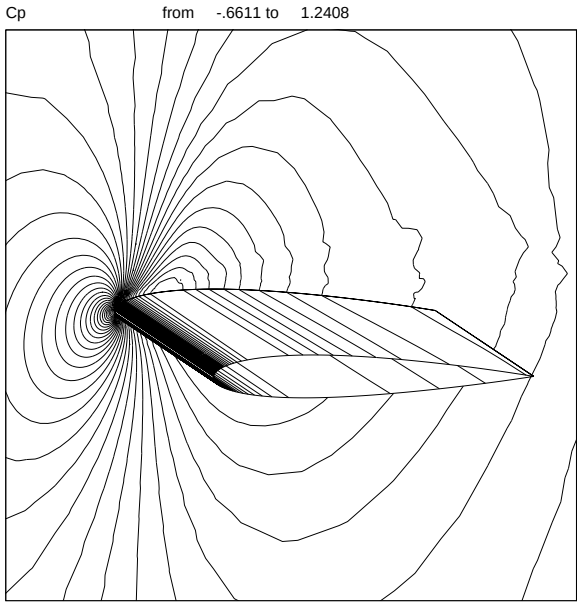

Figure 2: C_p distribution for NACA0012, Re=2000, $M_\infty = 0.8$, $\alpha = 3.5$ deg

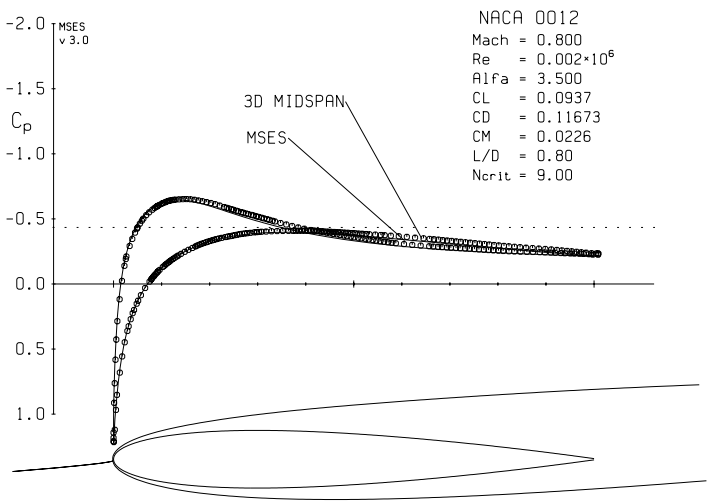

Figure 4: Surface C_p distribution for NACA0012, Re=2000, $M_\infty = 0.8$, $\alpha = 3.5$ deg: 3D NS solver midspan v. MSES

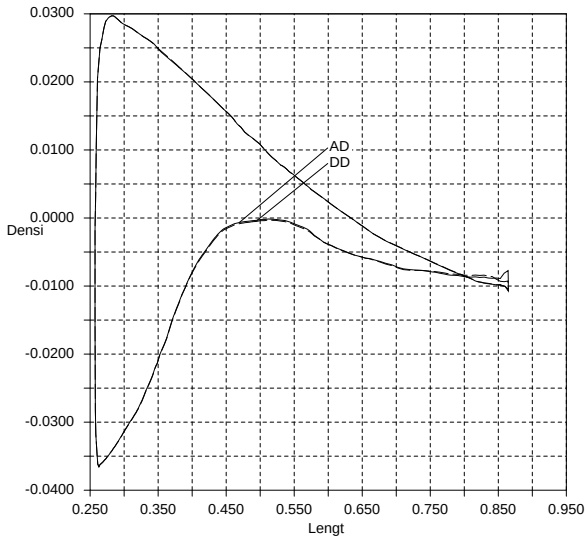

Figure 5: $\partial\rho/\partial\alpha$ distribution at midspan for NACA0012, Re=2000, $M_\infty = 0.8$, $\alpha = 3.5$ deg

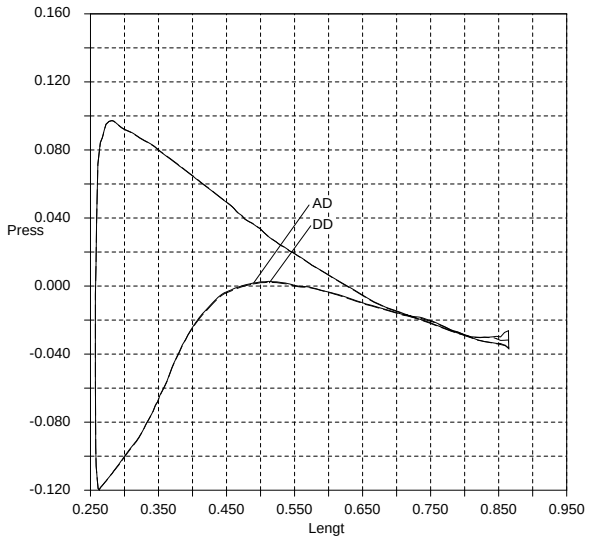

Figure 7: $\partial\rho E/\partial\alpha$ distribution at midspan for NACA0012, Re=2000, $M_\infty = 0.8$, $\alpha = 3.5$ deg

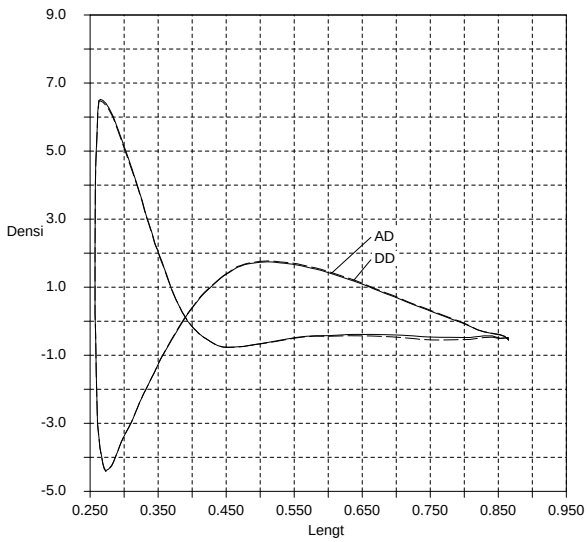

Figure 6: $\partial\rho/\partial\beta_c$ distribution at midspan for NACA0012, Re=2000, $M_\infty = 0.8$, $\alpha = 3.5$ deg

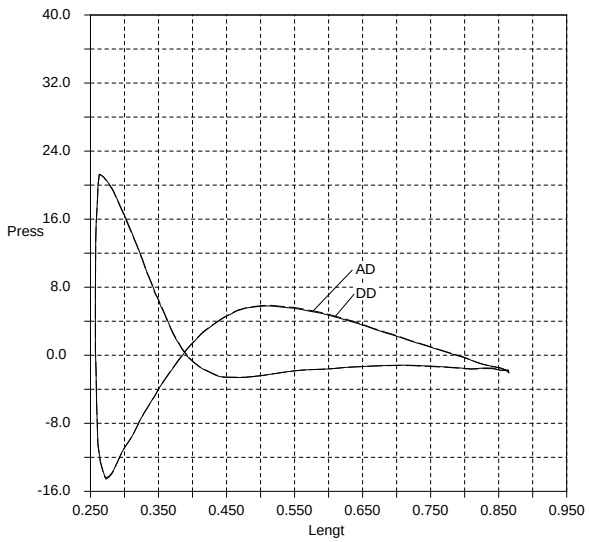

Figure 8: $\partial\rho E/\partial\beta_c$ distribution at midspan for NACA0012, Re=2000, $M_\infty = 0.8$, $\alpha = 3.5$ deg

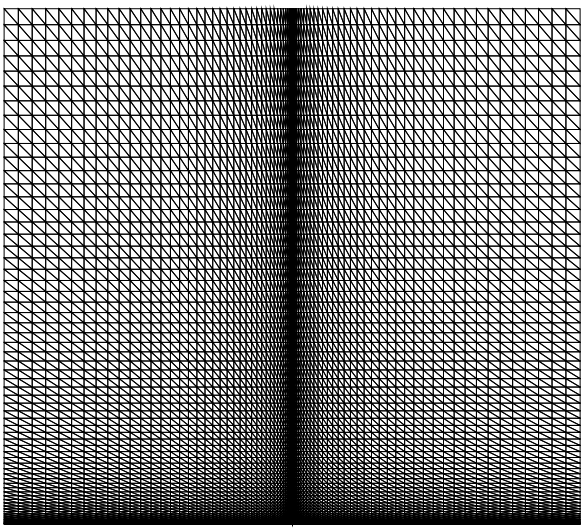

Figure 9: Grid used for flat plate calculation, plotted in domain $(\xi, \eta) = (x, y(Re/1000)^{1/2})$

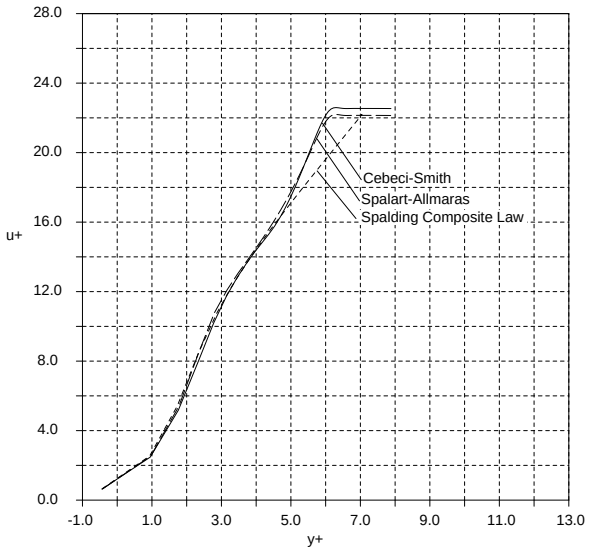

Figure 11: Comparison of velocity profiles at $x = 0.96$ Spalding composite law using inner variables

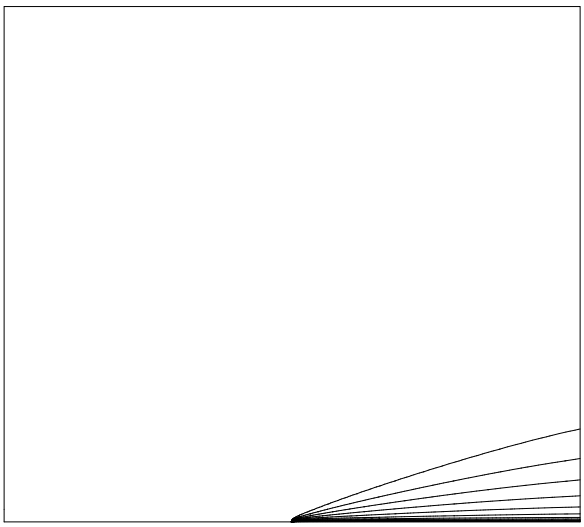

Figure 10: ρu distribution for flat plate calculation, plotted in domain $(\xi, \eta) = (x, y(Re/1000)^{1/2})$

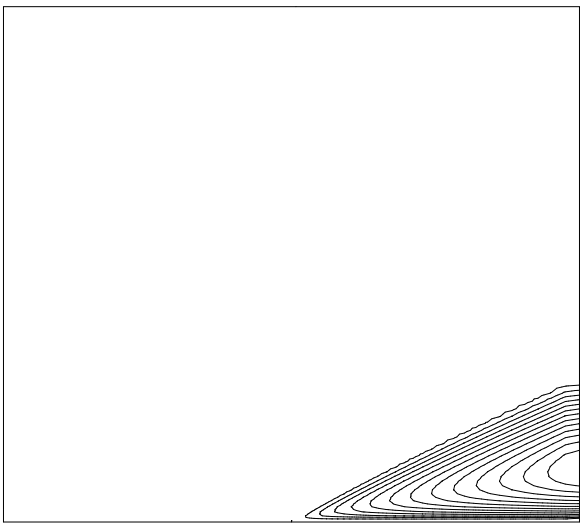

Figure 12: ν_t distribution for flat plate calculation, plotted in domain $(\xi, \eta) = (x, y(Re/1000)^{1/2})$

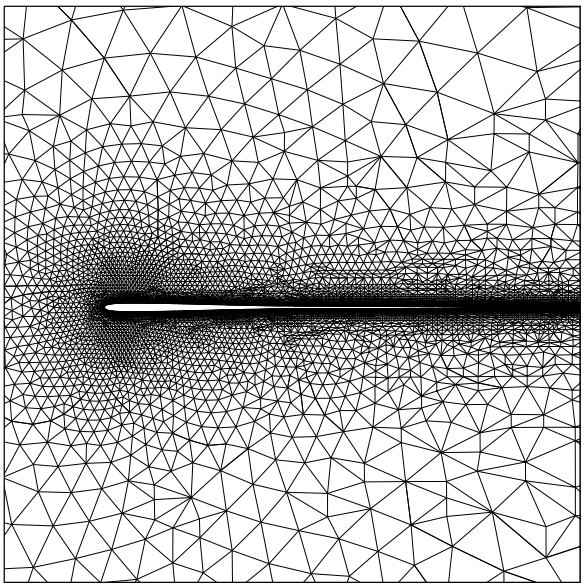

Figure 13: μ-UAV airfoil grid

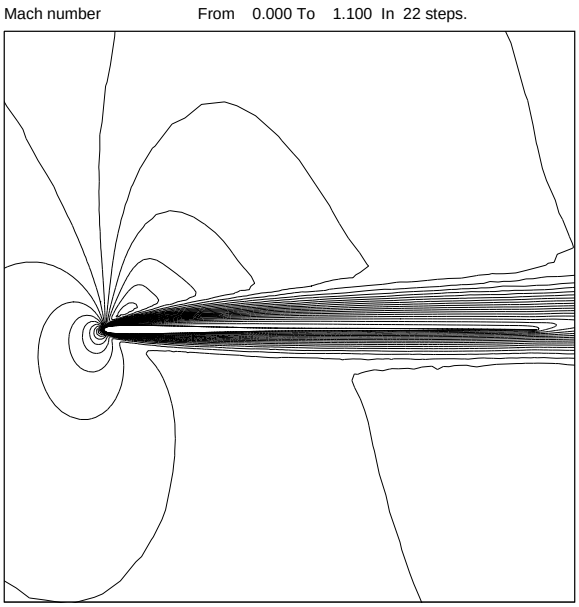

Figure 15: Baseline M distribution for μ-UAV airfoil, Re=2000, $M_\infty = 0.8$, $\alpha = 3.5$ deg

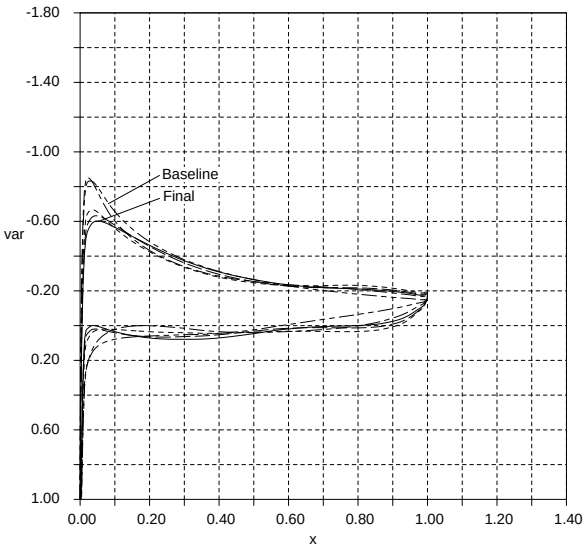

Figure 14: Surface C_p evolution for μ-UAV airfoil, Re=2000, $M_\infty = 0.8$, $\alpha = 3.5$ deg

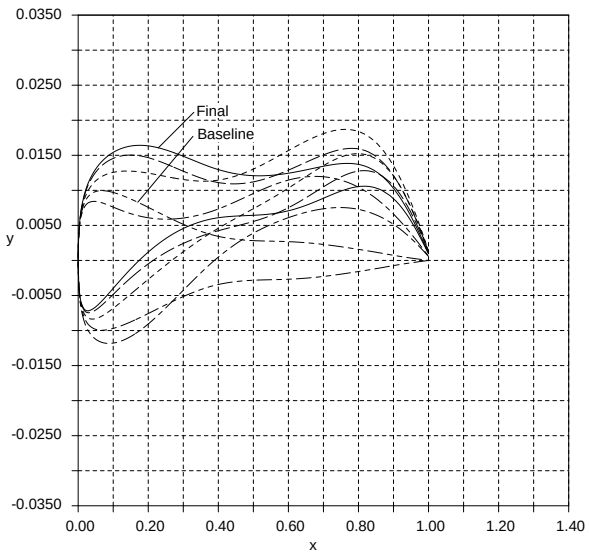

Figure 16: Geomety evolution for μ-UAV airfoil, Re=2000, $M_\infty = 0.8$, $\alpha = 3.5$ deg

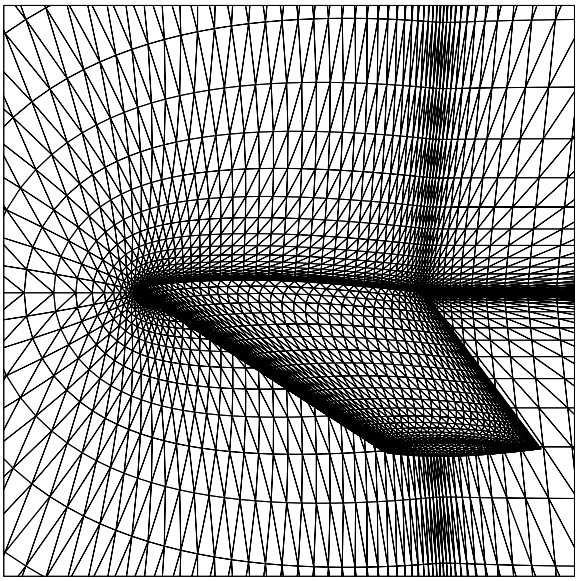

Figure 17: Surface grid for ONERA M6 calculation

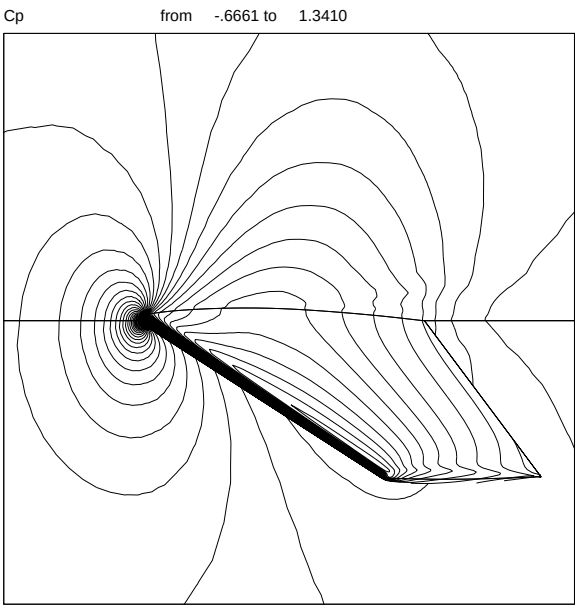

Figure 18: Baseline C_p distribution for ONERA M6 optimization exercise

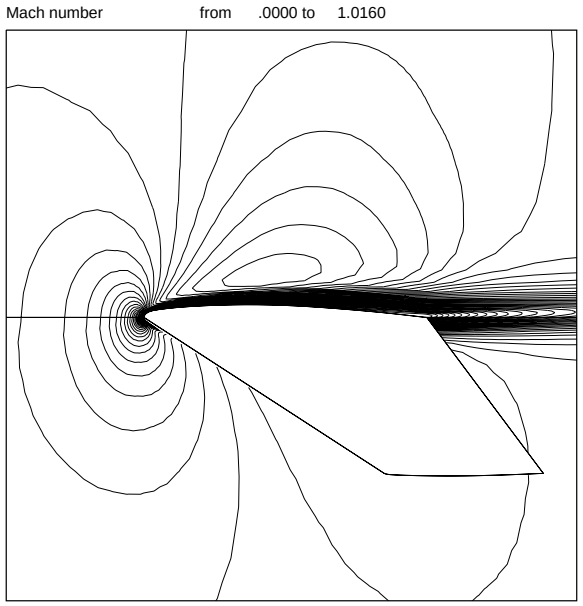

Figure 19: Baseline M distribution for ONERA M6 optimization exercise

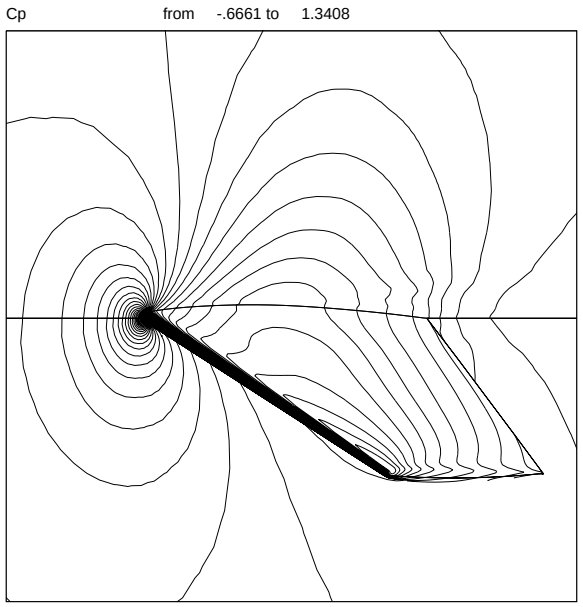

Figure 20: "Design 4" C_p distribution for ONERA M6 optimization exercise

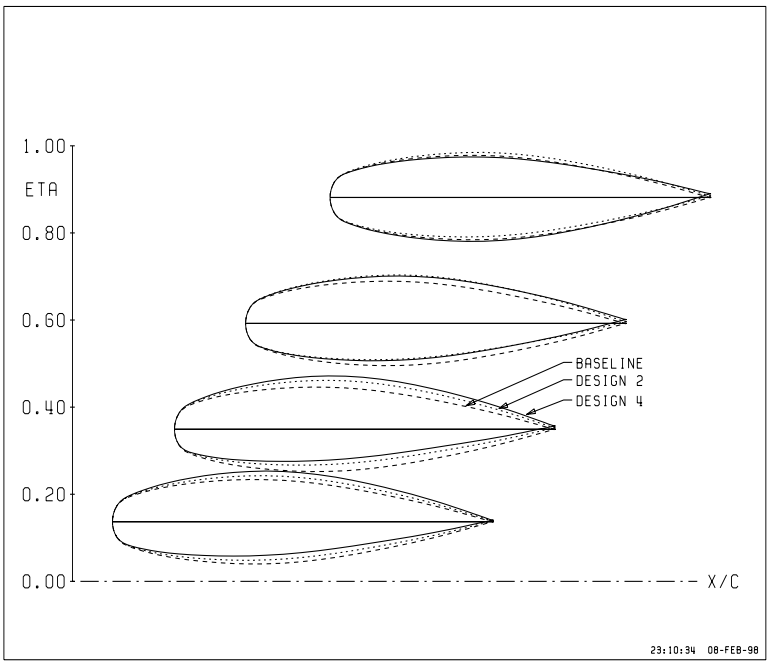

Figure 21: Geometry evolution for ONERA M6, Re=1600, $M_\infty = 0.8$, $\alpha = 3.5\,\mathrm{deg}$

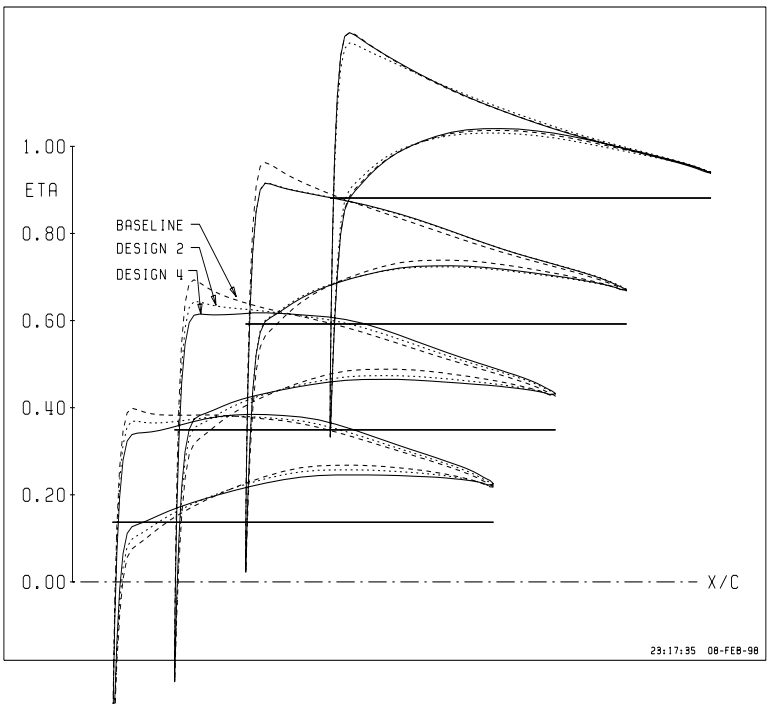

Figure 22: C_p evolution for ONERA M6, Re=1600, $M_\infty = 0.8$, $\alpha = 3.5\,\mathrm{deg}$

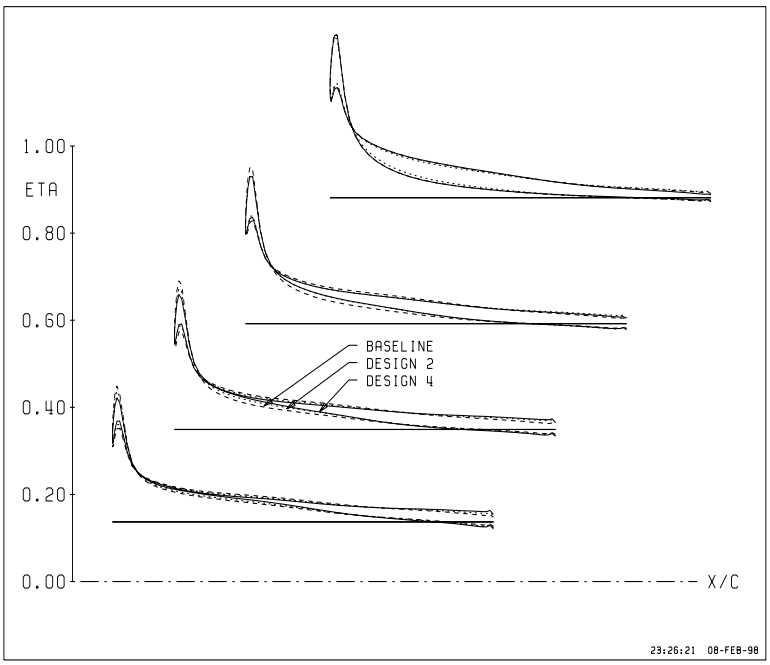

Figure 23: C_f evolution for ONERA M6, Re=1600, $M_\infty = 0.8$, $\alpha = 3.5$ deg

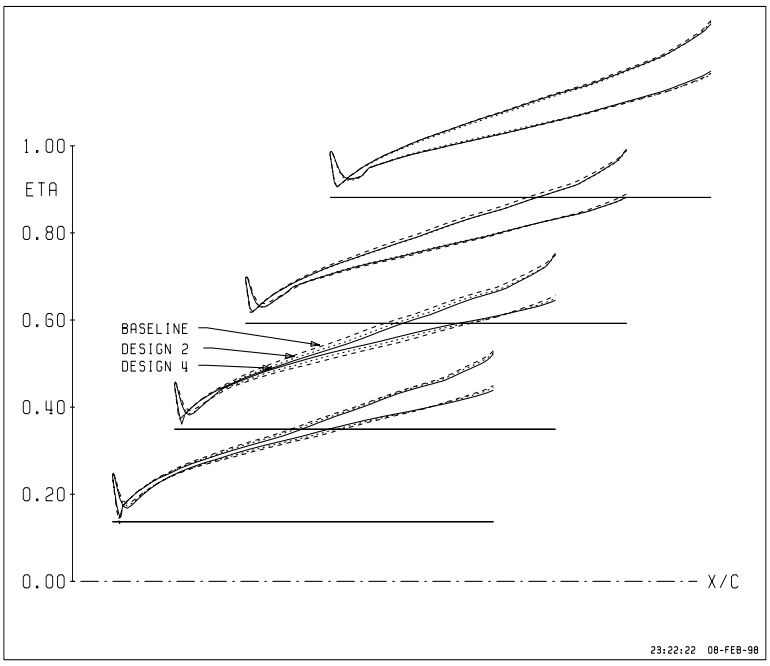

Figure 24: θ evolution for ONERA M6, Re=1600, $M_\infty = 0.8$, $\alpha = 3.5$ deg